J. Fluid Mech. (2008), *vol.* 595, *pp.* 435–459.
doi:10.1017/S0022112007009378 Printed in the United Kingdom

Investigation of the backflow phenomenon in falling liquid films

GEORG F. DIETZE†, A. LEEFKEN AND R. KNEER

Institute of Heat and Mass Transfer, RWTH Aachen University, Aachen, 52056, Germany

(Received 13 May 2007 and in revised form 27 September 2007)

The phenomenon of backflow in the capillary wave region of laminar falling liquid films is studied in detail. For the first time, the mechanism leading to the origination of the phenomenon is identified and explained. It is shown that backflow forms as the result of a separation eddy developing at the bounding wall similar to the case of classical flow separation. Results show that the adverse pressure distribution causing the separation of the flow in the capillary wave region is induced by the strong third-order deformation (i.e. change in curvature) of the liquid–gas free surface there. This deformation acts on the interfacial pressure jump, and thereby the wall pressure distribution, as a result of surface tension forces. It is shown that only the capillary waves, owing to their short wavelength and large curvature, impose a pressure distribution satisfying the conditions for flow separation. The effect of this capillary separation eddy on momentum and heat transfer is investigated from the perspective of modelling approaches for falling liquid films. The study is centred on a single case of inclined liquid film flow in the visco-capillary regime with surface waves externally excited at a single forcing frequency. Investigations are based on temporally and spatially highly resolved numerical data obtained by solving the Navier–Stokes equations for both phases. Computation of phase distribution is performed with the volume of fluid method and the effect of surface tension is modelled using the continuum surface force approach. Numerical data are compared with experimental data measured in the developed region of the flow. Laser-Doppler velocimetry is used to measure the temporal distribution of the local streamwise velocity component, and confocal chromatic imaging is employed to measure the temporal distribution of film thickness. Excellent agreement is obtained with respect to film thickness and reasonable agreement with respect to velocity.

1. Introduction

The mechanisms of momentum, heat and mass transfer in laminar falling liquid films have been the subject of numerous experimental, numerical and analytical investigations since the pioneering works of Nusselt (1916), Kapitza (1948), Brauer (1956), Benjamin (1957) and Wilke (1962). Their prevalence as a research topic is due to continuing technical relevance in nuclear (see e.g. Takase *et al.* 2003) and chemical engineering and the fact that much remains to be resolved concerning the transport mechanisms. On the one hand there is a need to develop a proper understanding of all relevant physical phenomena taking place in the liquid film; on the other hand,

† Present address: Institute of Heat and Mass Transfer, 18 Eilfschornsteinstrasse, Aachen, Germany.

adequate model structures need to be formulated, such that the relevant phenomena can be captured in an appropriate manner. The present work seeks to contribute to the former of these tasks by way of an experimental and numerical investigation into the backflow phenomenon occurring under certain conditions in the capillary-wave region of laminar falling liquid films. For the sake of clarity, it is noted here that backflow is to be understood as existing in a wall fixed coordinate system. The very existence of this phenomenon has been debated in the literature since Kapitza (1948) and Portalski (1964) proved, in principle, the possibility of flow reversal in falling liquid films. In these studies, the location of the backflow region is predicted to be at the wave trough which is a conclusion principally validated by the present work. However, in the present work, the presence of capillary waves there, which are not considered by Kapitza and Portalski, is found to be essential as only these provide the extreme conditions necessary to induce flow reversal.

Experimental proof of the backflow phenomenon was provided by Adomeit, Leefken & Renz (2000) in the form of particle path lines visualized with a laser at high pulse frequency. Results show particles following 'loop-shaped' trajectories in the capillary-wave region. Adomeit *et al.* also present numerical data revealing backflow in the capillary-wave region. Since then, the backflow phenomenon has been demonstrated in a number of purely numerical studies (e.g. Leefken & Renz 2001; Kunugi & Kino 2005; Kunugi, Kino & Serizawa 2005). These results, however, are limited by an insufficient spatial resolution of the liquid film in the capillary-wave region, where its thickness is of the order of 500 μm. In all these publications, the backflow phenomenon is considered exclusively in its developed state. Further, no explanation has ever been proposed for the origination and development of this phenomenon. These two shortcomings, which are relevant to each other, are addressed in the present work.

The backflow phenomenon is not only of academic interest as the resulting local flow conditions cause a significant intensification of heat transfer between the liquid and its bounding wall. Wave-induced intensification of heat transfer in falling liquid films as such has been demonstrated in numerous investigations and is widely accepted. For example, Frisk & Davis (1972) reported a 100 % increase of the temporally averaged Nusselt number in heated shear-driven wavy film flow compared to the corresponding smooth case. However, the identification of backflow in the capillary-wave region as a significant contributor to the intensification occurred only recently. Adomeit *et al.* (2000) show the concomitance of the backflow phenomenon and heat transfer intensification based on numerical data. They do not explicitly establish a link of causality between the two phenomena. This was later provided by Kunugi & Kino (2005) and Kunugi *et al.* (2005). The effect of the backflow phenomenon on the convective transfer processes in the capillary-wave region has not been analysed in detail owing to the lack of spatial resolution. Such an analysis is provided in the present paper.

Accurate models of wave dynamics based on long-wave theory have been published by Nguyen & Balakotaiah (2000), Ruyer-Quil & Manneville (2000), Scheid, Ruyer-Quil & Manneville (2006) and Mudunuri & Balakotaiah (2006). An essential assumption in their approach concerns the degree of freedom of polynomials assumed to represent the crosswise distribution of the streamwise velocity. Highly resolved numerical data in the capillary-wave region are required in order to provide a basis for the physical justification of such modelling assumptions.

Both the numerical and experimental methods employed in this study are established in the literature with respect to the investigation of falling liquid films.

Gao, Morley & Dhir (2003) first published numerical results concerning the fluid and wave dynamics of falling liquid films using the volume of fluid method developed by Hirt & Nichols (1981) for the computation of phase distribution and the interface reconstruction scheme published by Youngs (1982). The effect of surface tension forces is modelled with the continuum surface force method established by Brackbill, Kothe & Zemach (1992). The authors principally demonstrate the plausibility of numerical results by comparing these with experimental data produced by Kapitza & Kapitza (1965) and Alekseenko, Nakoryakov & Pokusaev (1994). In the present work the same methods are employed and subjected to a more detailed experimental validation.

Experimentally, in the current study, laser-Doppler velocimetry (LDV) and a confocal chromatic imaging method are employed to measure simultaneously the instantaneous local streamwise velocity and film thickness. The first LDV investigations of falling liquid films were published by Mudawar & Houpt (1993) whereby the film thickness was measured simultaneously using an invasive method. Characteristically, a sampling channel was employed to enable optical accessibility of the cross-section of the film flow for the front-scattering LDV configuration they employed. Leefken, Al-Sibai & Renz (2004) employed a back-scattering LDV set-up to measure the streamwise velocity component in a falling liquid film through a glass plate. Their results compare well with numerical data produced using the spectral element method for interface tracking and periodic boundary conditions. The confocal chromatic imaging method employed in this study was first used for film-thickness measurements in falling liquid films by Lel, Al-Sibai & Leefken (2005) although in a different configuration. In that study, film-thickness data from laser induced fluorescence measurements and from the confocal chromatic imaging method were cross-validated.

In the present study, the backflow phenomenon is investigated in detail on the basis of numerical data for one set of operating conditions in unprecedented spatial resolution validated by experimental results. For the first time, a mechanistic explanation of the origination and development of the backflow phenomenon is provided. Further, its effect on heat transfer from the bounding wall to the fluid is investigated. Results enable a general understanding of published experimental findings and could serve as a stepping stone for the development of adequate modelling approaches.

The paper is structured as follows. In § 2, the experimental approach is presented. The case considered in this study is defined in detail and the employed experimental techniques are introduced. The numerical approach is treated in § 3. The system of governing equations underlying the numerical analysis is introduced and the methods of numerical solution are described. Section 4 presenting the results of the study is partitioned into three subsections. First, data resulting from numerical simulation are compared to experimental data in § 4.1. In § 4.2.1, the origination and development of the backflow phenomenon is demonstrated and explained whereas § 4.2.2 treats the influence of the backflow phenomenon on heat transfer. Conclusions are drawn in § 5.

2. Experimental investigations

2.1. *Experimental conditions*

Figure 1 shows the experimental set-up defining the case of falling liquid film flow under consideration here. It consists of an acrylic glass plate, inclined at an angle ϕ to

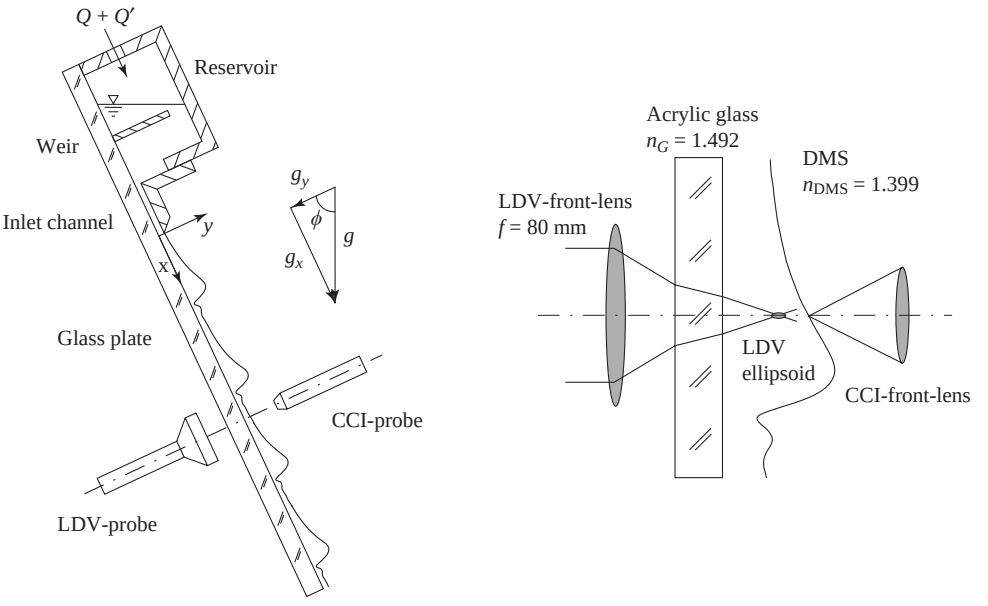

FIGURE 1. Experimental set-up.

δ_0 (μm)	W (mm)	ϕ(deg.)	ρ (kg m^{-3})	σ (N m^{-1})	μ (kg m^{-1}s^{-1})	λ (W m^{-1}K^{-1})	c (J kg^{-1} K^{-1})	f (s^{-1})	Q (m^3 s^{-1})
635	265	35	909.3	0.022	5.18×10^{-3}	0.12	1540	15	2.36×10^{-5}

TABLE 1. Dimensional parameters of the considered inclined liquid film flow (fluid properties measured at $T = 25°$ for particle-laden liquid).

the gravitational acceleration vector, on which the liquid develops into a falling film at the exit of a rectangular inlet channel with width W and variable channel height. The liquid is fed into the reservoir upstream of the inlet channel by a gear pump. A fluctuation Q' of frequency f and small amplitude is imposed on the mean feeding flow rate Q by way of a pressure fluctuation generated with a loud speaker (not pictured) upstream of the reservoir. To avoid direct perturbations at the inlet channel by the impinging liquid jet entering the reservoir, an obstructing weir is inserted. As working fluid, a liquid belonging to the group of dimethylsiloxanes (DMS) with the designation DMS-T05 is employed. The liquid is seeded with titanium dioxide particles acting as tracers for the LDV. The average diameter of the seeding particles is of the order of 10 μm and the density of the material of the order of 4500 kg m^{-3}. The properties of the particle-laden liquid were measured at the working temperature $T = 25\,°$C and are given in table 1.

The wave dynamics of the considered regime are characterized by two-dimensional solitary waves developing from the forced inlet disturbance with frequency f preceded by capillary waves and attaining a constant amplitude before secondary instability leads to their break up into three-dimensional structures. Alekseenko *et al.* (1994) introduce the term *stationary two-dimensional waves* to designate the regime in question. The term *capillary wave* is to be understood in the sense that the effect of surface tension dominates the effect of gravity, as stated by Whitham (1974). In the context of this study only the region of development of the two-dimensional waves

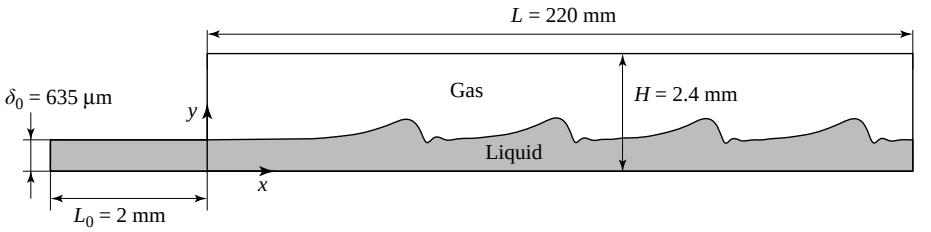

FIGURE 2. Computational domain.

is considered. In the experiments as well as in the numerical simulation, the height δ_0 of the inlet channel (the channel height is illustrated in figure 2) was set to the value of the film thickness δ_{Nu} for the corresponding smooth developed film flow (the subscript refers to the work of Nusselt 1916):

$$\delta_{Nu} = \left[\frac{3\,q\,\nu_l}{g_x}\right]^{1/3}, \quad q = \frac{Q}{W}, \tag{2.1}$$

whereby q designates the mean volume flow rate per unit width. This choice is motivated by the focus of the investigation. As will be shown subsequently, the backflow phenomenon is governed by the dynamics of the capillary waves and forms before these attain their developed state. Thus, the region of wave development of the flow is of primary interest. Alekseenko *et al.* (1994) show, for smooth film flow, that for a given inlet height, the film thickness tends to δ_{Nu} in the streamwise direction, which also applies to the wavy flow as far as the mean film thickness is concerned (see e.g. Lel *et al.* 2005) for laminar regimes dominated by viscous and capillary forces. Thus, by setting $\delta_0 = \delta_{Nu}$ an unnecessary streamwise change in the mean film thickness is avoided, thereby isolating the wave-development process relevant to the backflow phenomenon. However, it should be noted that owing to the discontinuous change in boundary conditions at the inlet (not considered by Alekseenko *et al.* 1994) a certain streamwise development of the mean flow still takes place.

2.2. *Measurement of instantaneous streamwise velocity*

For the measurement of the streamwise velocity component a standard two-component LDV system in back-scattering configuration was employed. The system allows for the simultaneous measurement of the streamwise and spanwise velocity components comprising a two-component fibre optic probe with back-scatter collection optics and two burst spectrum analysers. The spanwise component was measured only for preliminary alignment purposes as non-zero values point to misalignment in the considered two-dimensional flow. Only the measurement of the streamwise component is addressed here. A description of laser-Doppler velocimetry is given by Albrecht *et al.* (2003) and our explanation concentrates on the aspects specific to measurements in falling liquid films. The seeded flow is accessed optically through the bounding acrylic glass plate without disturbing the falling film (figure 1) as opposed to the set-up used by Mudawar & Houpt (1993). The principal disadvantage of the configuration results from the shape of the measurement ellipsoid constituting the intersection volume of the laser beams. The major axis of the ellipsoid is oriented in the y-direction in which the principal velocity variation takes place, leading to resolution problems. The two parallel laser beams creating the measurement ellipsoid are of wavelength 514.5 nm and diameter 2.2 mm and are focused by an achromatic lens of focal length 80 mm. The resulting intersection angle in the liquid is 19.02°,

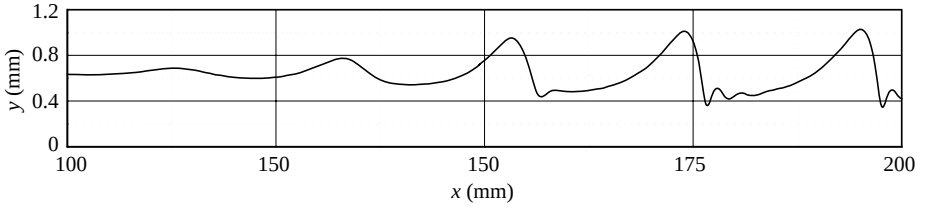

FIGURE 3. Computed spatial evolution of surface waves for a given time.

taking into account the double refraction of the LDV beams. The dimensions of the measurement ellipsoid in the x and y directions then are 24 μm and 144 μm, respectively. As will be shown in subsequent sections (see figure 3) the minimal film thickness of the considered flow is of the order of 300 μm leading to a minimal film thickness to ellipsoid height ratio of 2. Elsässer (1998) used separate receiving optics equipped with a 25 μm slit aperture reducing the size of the imaged measurement volume to perform measurements in very thin shear-driven films. The mentioned ratio thereby was of the same order as in the present study. Mudawar & Houpt (1993), owing to the use of an invasive sampling channel and the investigation of flow regimes characterized by large film thickness, were able to achieve significantly higher resolution. As the purpose of the experimental investigation is principally the validation of numerical data, the encountered variance of experimental data due to intermediate spatial resolution is not prohibitive. The lagging behaviour of the titanium dioxide seeding particles was quantified based on the solution of the Basset–Boussinesq–Oseen equation in Hjemfelt & Mockros (1966). Results show that at flow oscillation frequencies of up to 10,000 Hz, the deviation of particle kinematics from flow kinematics is negligible.

2.3. *Measurement of instantaneous film thickness*

For the measurement of local film thickness, the confocal chromatic imaging technique developed by Cohen-Sabban, Gaillard-Groleas & Crepin (2001) for surface sensing was employed. The system comprises a fibre optic probe focusing white light onto an interval of foci with a chromatic front lens. The technique enables the measurement of the distance along the optical axis between a given reflecting surface and a fixed reference point. The spectral distribution of light reflected by the surface is analysed with a spectrometer yielding the distance information. A more detailed description can be found in Cohen-Sabban *et al.* (2001). The distance measurement error is of the order of 1 μm. Film thickness was determined as the difference between the instantaneously measured distance to the liquid–gas free surface (subsequently simply referred to as the interface) and the distance to the acrylic glass plate measured prior to film development. The resulting upper bound for the film thickness measurement error then is 2 μm. The fibre optic probe is positioned such that its optical axis is parallel to that of the LDV probe (figure 1). Both optical axes thereby lie in the same plane parallel to the (y, z)-plane. However, the probes are 5 mm apart in the z-direction to avoid damage to the CCI device by the laser beams. Measurements were performed with a sampling frequency of 800 Hz temporally resolving each surface wave with 50 data points. The spatial resolution of the film-thickness measurement in the x-direction is defined by the coupling of transmitting optics and the spectrometer and is of the order of 10 μm. Velocity and film-thickness measurements were performed simultaneously.

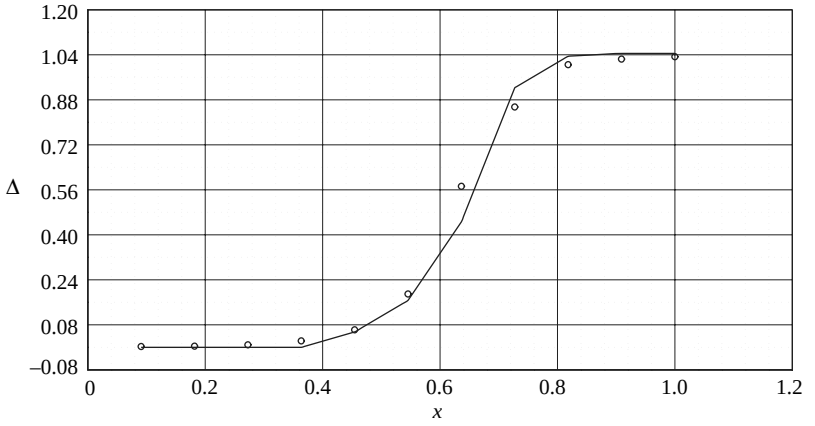

FIGURE 4. Streamwise spatial evolution of wave amplitude. ○, experiment; —, simulation.

3. Numerical investigations

Two numerical investigations were performed in the present study. The main investigation is purely fluid-dynamical and seeks to reproduce as accurately as possible the experimental conditions described in § 2. The second investigation focuses on the effect of the backflow phenomenon on heat transfer for identical fluid-dynamical conditions. For all numerical investigations, the film flow is considered as two-dimensional, laminar and incompressible with constant fluid properties evaluated at $T = 25\,^{\circ}\mathrm{C}$ (the influence of heat transfer on momentum transfer is neglected). Liquid properties are given in table 1. Properties of air constituting the atmosphere of the liquid film were evaluated at the reference static pressure $p_r = 101\,325\,\mathrm{Pa}$ and are not listed here. The computational domain considered for the numerical investigations (figure 2) includes a portion of the inlet channel. The length of the retained portion of the inlet channel is chosen, such that the mean velocity field at the inlet of the computational domain can be considered as developed. Length and height of the two-phase region of the computational domain were defined on the basis of experimental film-thickness data. The length is chosen to include the entire developing region of surface waves (see e.g. figure 4), and the height as roughly twice the maximal thickness of the developed surface waves. That these conditions are met can be deduced from figure 3, depicting the instantaneous spatial distribution of film thickness for a given time as obtained by numerical simulation.

3.1. *Governing equations*

The flow in both the gaseous and the liquid phase is governed by the Navier–Stokes equations and the continuity equation written here in non-dimensional form:

$$\frac{\partial u^*}{\partial t^*} + u^* \frac{\partial u^*}{\partial x^*} + v^* \frac{\partial u^*}{\partial y^*} = -\gamma \frac{\partial p^*}{\partial x^*} + \frac{\chi}{Re}\left(\epsilon \frac{\partial^2 u^*}{\partial x^{*2}} + \frac{1}{\epsilon}\frac{\partial^2 u^*}{\partial y^{*2}}\right) + \frac{3\chi}{\epsilon\, Re}, \tag{3.1a}$$

$$\frac{\partial v^*}{\partial t^*} + u^* \frac{\partial v^*}{\partial x^*} + v^* \frac{\partial v^*}{\partial y^*} = -\frac{\gamma}{\epsilon^2} \frac{\partial p^*}{\partial y^*} + \frac{\chi}{Re}\left(\epsilon \frac{\partial^2 v^*}{\partial x^{*2}} + \frac{1}{\epsilon}\frac{\partial^2 v^*}{\partial y^{*2}}\right) + \frac{1}{\epsilon\, Fr^2}, \tag{3.1b}$$

$$\frac{\partial u^*}{\partial x^*} + \frac{\partial v^*}{\partial y^*} = 0, \tag{3.1c}$$

where χ and γ have been introduced to distinguish the formulations for the respective phases. In the gaseous phase $\chi = \Pi_\mu/\Pi_\rho$, $\gamma = 1/\Pi_\rho$ and in the liquid phase $\chi = \gamma = 1$

with the density ratio $\Pi_\rho = \rho_g/\rho_l$ and the dynamic viscosity ratio $\Pi_\mu = \mu_g/\mu_l$. The subscripts g and l refer to the gaseous and liquid phase, respectively. As the atmosphere of the falling liquid film is quiescent gas, the scales in both the liquid and the gaseous phase are imposed by the flow in the liquid phase:

$$x^* = \frac{x}{L},\ y^* = \frac{y}{\delta_{Nu}},\ t^* = \frac{t u_{Nu}}{L},\ p^* = \frac{p}{\rho_l u_{Nu}^2},\ u^* = \frac{u}{u_{Nu}},\ v^* = \frac{v}{u_{Nu}}\frac{L}{\delta_{Nu}}, \tag{3.2}$$

with the mean velocity $u_{Nu} = (g_x \delta_{Nu}^2)/(3\nu_l)$ for smooth developed film flow. The dimensionless Navier–Stokes and continuity equations yield the Reynolds number Re, the Froude number Fr and the ratio of length scales ϵ:

$$Re = \frac{u_{Nu}\,\delta_{Nu}}{\nu_l}, \quad Fr = \frac{u_{Nu}}{(g_y\,\delta_{Nu})^{1/2}}, \quad \epsilon = \frac{\delta_{Nu}}{L}. \tag{3.3}$$

Assuming constant surface tension, the normal and tangential coupling conditions at the interface $y = \delta$ between gaseous and liquid phase are:

$$\begin{aligned} &p_l^* - p_g^* + \frac{We\,\epsilon^2}{\beta^{3/2}}\frac{\partial^2\delta^*}{\partial x^{*2}} \\ &\quad = \frac{2\epsilon}{\beta\, Re_l}\left[\epsilon^2\frac{\partial u_l^*}{\partial x^*}\left(\frac{\partial\delta^*}{\partial x^*}\right)^2 + \frac{\partial v_l^*}{\partial y^*} + \frac{\partial\delta^*}{\partial x^*}\left(\frac{\partial u_l^*}{\partial y^*} + \epsilon^2\frac{\partial v_l^*}{\partial x^*}\right)\right] \\ &\qquad - \frac{2\epsilon\,\Pi_\mu}{\beta\, Re_l}\left[\epsilon^2\frac{\partial u_g^*}{\partial x^*}\left(\frac{\partial\delta^*}{\partial x^*}\right)^2 + \frac{\partial v_g^*}{\partial y^*} + \frac{\partial\delta^*}{\partial x^*}\left(\frac{\partial u_g^*}{\partial y^*} + \epsilon^2\frac{\partial v_g^*}{\partial x^*}\right)\right], \end{aligned} \tag{3.4}$$

$$\begin{aligned} &\epsilon\frac{\partial\delta^*}{\partial x^*}\left(\frac{\partial u_l^*}{\partial x^*} - \frac{\partial v_l^*}{\partial y^*}\right) + \left(\frac{\beta}{2} - 1\right)\frac{\partial\delta^*}{\partial x^*}\left(\frac{\partial u_l^*}{\partial y^*} + \epsilon^2\frac{\partial v_l^*}{\partial x^*}\right) \\ &\quad = \Pi_\mu\,\epsilon\frac{\partial\delta^*}{\partial x^*}\left(\frac{\partial u_g^*}{\partial x^*} - \frac{\partial v_g^*}{\partial y^*}\right) + \Pi_\mu\left(\frac{\beta}{2} - 1\right)\frac{\partial\delta^*}{\partial x^*}\left(\frac{\partial u_g^*}{\partial y^*} + \epsilon^2\frac{\partial v_g^*}{\partial x^*}\right), \end{aligned} \tag{3.5}$$

whereby the following definitions are introduced:

$$We = \left[\frac{3\,\sigma^3\,\nu_l}{\rho_l^3\, g_x\, q^5}\right]^{1/3}, \quad \beta = 1 + \epsilon^2\left(\frac{\partial\delta^*}{\partial x^*}\right)^2, \quad \delta^* = \frac{\delta}{\delta_{Nu}}, \tag{3.6}$$

and We designates the Weber number. It should be repeated here that δ_{Nu} is related to the main control parameter q by (2.1). The local instantaneous film thickness δ is related to the velocity field through the kinematic condition:

$$v^*|_{y^*=1} = \frac{\mathrm{d}\delta^*}{\mathrm{d}t^*}, \tag{3.7}$$

which states that the crosswise displacement velocity of the interface corresponds to the crosswise liquid velocity at the interface. The numerical problem is closed with the following boundary conditions:

$$u^*|_{x^*=-\xi_L} = 6(y^* - y^{*2})(1 + \varepsilon\,\sin(2\pi\,\Pi_f\,t^*))\forall y^* \in]0, \xi_\delta], \tag{3.8a}$$

$$v^*|_{x^*=-\xi_L} = 0\ \forall y^* \in]0, \xi_\delta],\ u^*|_{y^*=0} = v^*|_{y^*=0} = 0\ \forall x^* \in]-\xi_L, 1], \tag{3.8b}$$

$$u^*|_{y^*=\xi_\delta} = v^*|_{y^*=\xi_\delta} = 0\ \forall x^* \in]-\xi_L, 0],\ p^*|_{x^*=1} = p_r^*\ \forall y^* \in]0, \xi_H], \tag{3.8c}$$

$$u^*|_{y^*=\xi_H} = 0\,\forall x^* \in]0, 1],\ v^*|_{y^*=\xi_H} = \Pi_\rho^{-1}\,(p_r^* - p^*|_{y^*=\xi_H})^{0.5}\,\forall x^* \in]0, 1], \tag{3.8d}$$

$$v^*|_{x^*=0} = 0\,\forall y^* \in]\xi_\delta, \xi_H],\ u^*|_{x^*=0} = \Pi_\rho^{-1}\,(p_r^* - p^*|_{x^*=0})^{0.5}\,\forall y^* \in]\xi_\delta, \xi_H] \tag{3.8e}$$

Re	We	Fr	Π_f	δ_{Nu}/L	δ_0/δ_{Nu}	Pr
15.6	2.1	1.8	24.0	0.0029	0.98	66.5

TABLE 2. Non-dimensional parameters of the considered inclined liquid film flow.

where the dimensionless frequency Π_f and the geometric parameters ξ_δ, ξ_L and ξ_H are introduced:

$$\Pi_f = \frac{f\,L}{u_{Nu}}, \quad \xi_\delta = \frac{\delta_0}{\delta_{Nu}}, \quad \xi_L = \frac{L_0}{L}, \quad \xi_H = \frac{H}{\delta_{Nu}}. \tag{3.9}$$

Owing to the small height to length ratio of the inlet channel in the experimental set-up, a developed velocity profile at the inlet of the calculation domain is assumed. The value of the relative amplitude of the inlet disturbance ε was chosen such that the spatial evolution of the surface-wave amplitude obtained from the numerical simulation corresponds to experimental data.

For the heat transfer investigation, the governing system described in (3.1) is extended by the energy equation:

$$\frac{\partial \Theta^*}{\partial t^*} + u^* \frac{\partial \Theta^*}{\partial x^*} + v^* \frac{\partial \Theta^*}{\partial y^*} = \frac{\chi\,\epsilon}{Pr\,Re}\left(\frac{\partial^2 \Theta^*}{\partial x^{*2}} + \frac{1}{\epsilon^2}\frac{\partial^2 \Theta^*}{\partial y^{*2}}\right), \tag{3.10}$$

where in the gaseous phase $\chi = \Pi_\alpha$ and in the liquid phase $\chi = 1$, with the thermal diffusivity ratio $\Pi_\alpha = \alpha_g/\alpha_l$, the Prandtl number Pr and the dimensionless temperature difference Θ^*:

$$Pr = \frac{\nu_l\,\rho_l\,c_l}{\lambda}, \quad \Theta^* = \frac{T - T_0}{T_w - T_0}, \tag{3.11}$$

whereby the ambient temperature $T_0 = 300\,\mathrm{K}$ and the wall temperature $T_w = 350\,\mathrm{K}$. The coupling condition for the temperature field results from an interfacial heat balance:

$$-\frac{\partial \Theta_l^*}{\partial x^*}\frac{\partial \delta^*}{\partial x^*} + \frac{1}{\epsilon}\frac{\partial \Theta_l^*}{\partial y^*} = -\Pi_\lambda \frac{\partial \Theta_g^*}{\partial x^*}\frac{\partial \delta^*}{\partial x^*} + \frac{\Pi_\lambda}{\epsilon}\frac{\partial \Theta_l^*}{\partial y^*}, \tag{3.12}$$

introducing the thermal conductivity ratio $\Pi_\lambda = \lambda_g/\lambda_l$. Further, the following boundary conditions for the temperature field were considered:

$$\Theta^*|_{y^*=0} = 1\ \forall x^* \in]-\xi_L, 1], \quad \left.\frac{\partial \Theta^*}{\partial y^*}\right|_{y^*=1} = 0\ \forall x^* \in]-\xi_L, 0], \tag{3.13a}$$

$$\Theta^*|_{x^*=-\xi_L} = 0\ \forall y^* \in]0, 1], \quad \left.\frac{\partial \Theta^*}{\partial x^*}\right|_{x^*=1} = 0\ \forall y^* \in]0, \xi_H], \tag{3.13b}$$

$$\Theta^*|_{x^*=0} = 0\ \forall y^* \in]1, \xi_H], \quad \Theta^*|_{y^*=\xi_H} = 0\ \forall x^* \in]0, 1]. \tag{3.13c}$$

Table 2 gives values for the relevant characteristic dimensionless groups introduced in this section. As evidenced by the value of the Weber number, which relates viscous and capillary forces to gravitational and inertial forces, the considered regime is dominated by viscous and capillary forces.

3.2. *Numerical method*

The computational domain is spatially discretized with a structured Cartesian grid in the x- and y-directions. Dimensionless height (Δ_y) and length (Δ_x) of the resulting

rectangular control faces (non-dimensionalized with the respective length scales introduced in § 3) are defined as follows:

$$\Delta_x = 2.273 \times 10^{-4}, \tag{3.14a}$$

$$\Delta_y = \begin{cases} 0.031 & \forall y \leqslant 1.855, \\ 0.062 & \forall y > 1.855. \end{cases} \tag{3.14b}$$

The chosen control-face dimensions result from a grid-dependence analysis of the numerical solution. They were identified as adequate for the resolution of all relevant scales of the flow and proved to yield adequate numerical accuracy. Results are included in the next section (see figure 9). The discretization in time was realized in the fully implicit formulation with a dimensionless time step of $\Delta_t = 3.130 \times 10^{-6}$ (non-dimensionalized with the time scale introduced in § 3).

The governing equations of the film flow were solved on the computational domain (figure 2) using the volume of fluid (VOF) method based on the one-fluid approach to multiphase systems. The governing equations are thereby written for a single fluid defined on the entire computational domain. The multi-phase character of the real system is accounted for by formulating the properties of this single fluid as a function of phase distribution, quantified with the local volume fraction $\varphi = V^l/(V^l + V^g)$ of the liquid, and properties of the different phases (for details see e.g. Hirt & Nichols 1981). Thereby, the volume fraction φ is governed by the continuity equation for the liquid phase for the considered case of non-interpenetrating incompressible fluids:

$$\frac{\partial \varphi}{\partial t} + u \frac{\partial \varphi}{\partial x} + v \frac{\partial \varphi}{\partial y} = 0. \tag{3.15}$$

This equation is solved numerically in addition to the momentum and integral continuity equations. The employed discretization method and solution procedure are presented in detail in Youngs (1982). To simulate the effect of surface tension in the context of the VOF method, the continuum surface force (CSF) approach (for details see Brackbill *et al.* 1992) is employed. With respect to the numerical solution of the energy equation, no special treatment is necessary at the interface as the normal heat flux is continuous over the interface (see (3.12)). The governing equations are discretized using the finite-volume approach and solved with the pressure implicit split operator (PISO) method with fully implicit time stepping. The transport equation (3.15) is solved between solution iterations of the governing equations, using the velocity distribution from the current iteration step.

4. Results and discussion

Figure 3 shows surface waves developing on the smooth film leaving the inlet channel. The waves grow in size attaining constant shape and spacing as they travel downstream. Surface waves are characterized by large wave crests preceded by capillary waves of small amplitude and wavelength. In the following, these numerical results are compared to different experimental data in order to show their accuracy before the backflow phenomenon is investigated numerically. Unless otherwise stated all quantities employed subsequently are written in non-dimensional form whereby the star superscript employed previously is omitted.

4.1. *Comparison of numerical and experimental data*

Figure 4 compares the spatial evolution of wave amplitude in the streamwise direction obtained from experiment and numerical simulation, respectively. The wave amplitude

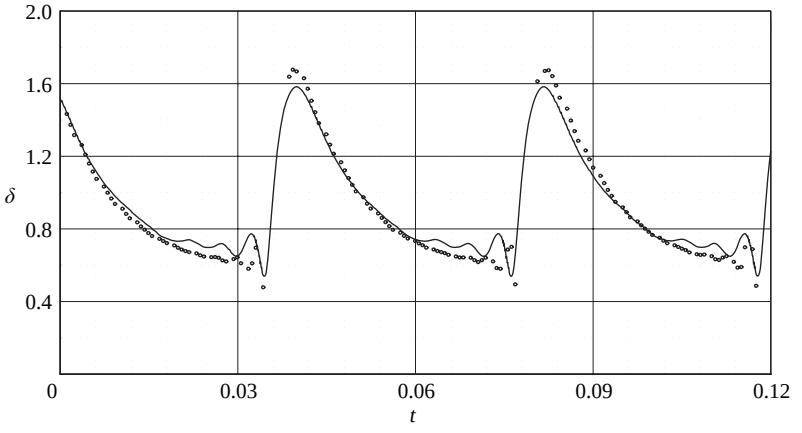

FIGURE 5. Film thickness time traces of developed surface waves. ●, experiment; —, simulation.

Δ is thereby defined as follows:

$$\Delta = \max\{\delta|_x\} - \min\{\delta|_x\}. \tag{4.1}$$

At a given point, Δ was determined from experimental data as the difference between the 95th and 5th percentile of the probability density function of local film thickness data. Numerical and experimental data are in good agreement so that it can be concluded that the region of development of surface waves is captured accurately in the simulation. It can be discerned in figure 4 that the surface waves attain their maximal amplitude at approximatively $x = 0.82$, thereby inside the computational domain (as mentioned in § 3). In figure 5, experimental and numerical data are compared with respect to the temporal evolution of the film thickness of developed waves yielding good agreement. Given the accuracy and simplicity of the film thickness measurement, this can be understood as a validation of the numerical method in the sense of adequacy of the chosen temporal and spatial discretization. In particular, the number, period length and amplitude of the capillary waves are predicted accurately by the numerical simulation. This will be of relevance when the backflow phenomenon is addressed.

Figure 6 depicts time traces of the streamwise velocity component obtained from experiment and numerical simulation, respectively. Data are evaluated in the region of developed surface waves for three different positions in the y-direction. One in the residual layer, one in the top of the wave crest and one intermediate position. The corresponding time trace of the simultaneously measured film thickness is also included in order to facilitate the interpretation of the velocity data. Agreement between experimental and numerical velocity data is good. Next to quantitative agreement, the shape of the time traces is predicted accurately by the simulation. In particular, the minimal peak of the velocity time trace in the residual layer is predicted. Figure 6(a) shows the streamwise velocity component decreasing there to values close to zero. This peak coincides with the capillary waves and is associated with the existence of the capillary separation eddy which strongly influences the flow at the considered crosswise position, as will be shown later (see figure 8a). In figures 6(b) and 6(c), the velocity time traces are truncated because the LDV measurement volume lies outside of the residual layer thereby only intermittently intersecting the liquid phase.

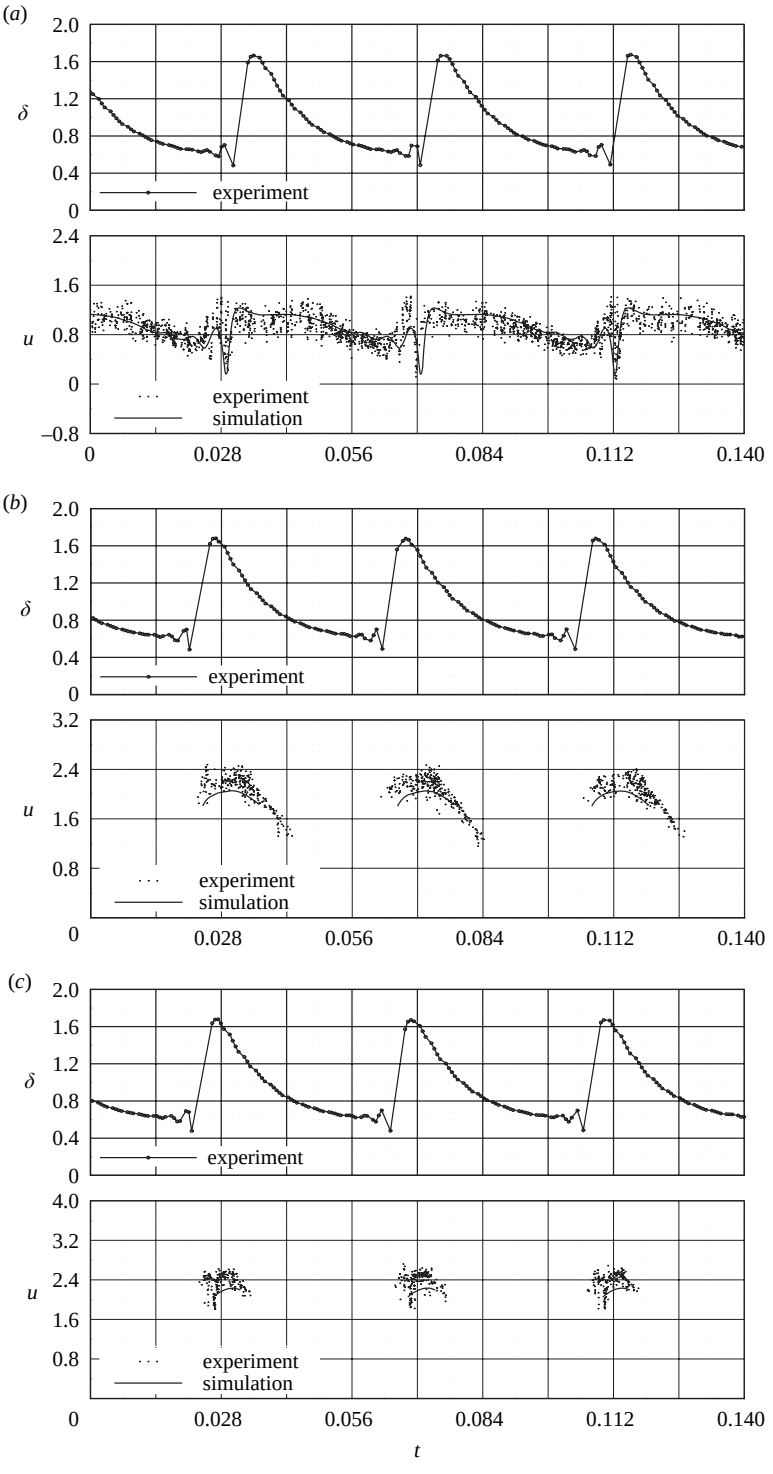

FIGURE 6. Streamwise velocity time traces for developed surface waves. (*a*) Residual layer: $y = 0.309$; (*b*) intermediate position: $y = 0.921$; (*c*) top of the wave crest: $y = 1.227$.

In summary, it can be stated that the simulation is sufficiently accurate in its spatial and temporal resolution, to base the ensuing analysis of the backflow phenomenon on numerical data. It has been shown for the case considered that wave dynamics in the developing region and in the region of developed film flow are accurately predicted by the simulation as well as momentum transfer in the developed film flow.

4.2. *Capillary separation eddy*

4.2.1. *Explanation of the development mechanism*

After the agreement between numerical and experimental data has been demonstrated, attention here is directed towards understanding the phenomenon of backflow in the capillary wave region. This is done on the basis of numerical data, exploiting their superior spatial resolution. In order to obtain a topological understanding of the phenomenon, streamlines of the flow in the capillary wave region along with the gas–liquid interface are shown in figures 7(*a*), 7(*c*) and 8(*a*) for different points in time. Figures 7(*b*), 7(*d*) and 8(*b*) depict the corresponding profiles of the streamwise velocity component at different streamwise positions in the vicinity of the wave trough. The streamline patterns show that backflow is the effect of an eddy developing at the wall in the capillary wave region. This eddy is the result of detachment and subsequent reattachment of the wall-bounded flow similar to classical flow separation. Thus it is designated as capillary separation eddy (CSE). The observed structure of the flow in the capillary wave region thereby validates the scenario proposed by Portalski (1964). Further, visualization experiments performed by Davies (1961) and Friedman & Miller (1941) reveal that the capillary phenomena of planar waves are essentially two-dimensional. Turbulent transport can therefore be excluded and the two-dimensional simulation performed suffices to resolve the backflow phenomenon.

The CSE phenomenon can be subdivided into three developmental episodes that are linked to the evolution of the surface wave. Figure 7(*a*) depicts near-wall streamlines of the flow shortly before separation occurs. A streamwise deceleration of the flow is noticeable as evidenced by the shape of the streamlines there. Indeed, tracked in the streamwise direction, the streamlines move away from the wall before re-approaching it. They attain their maximal distance from the wall slightly downstream of the wave trough. As for a given time the volume flow per unit width between two streamlines is constant, this behaviour is associated with a streamwise deceleration and re-acceleration of the mean flow in the near-wall region. This is more clearly identifiable when investigating the corresponding profiles of the streamwise velocity component. Figure 7(*b*) shows a significant deceleration (from $x = 0.7410$ to $x = 0.7430$) and re-acceleration (from $x = 0.7430$ to $x = 0.7456$) of the flow. As evidenced by comparison of the profiles at $x = 0.7410$ and $x = 0.7430$, the deceleration is associated with a sign change of the second-order crosswise derivative from negative to positive near the wall. This is due to the stronger deceleration of fluid elements closer to the wall with lower kinetic energy leading to a near-wall turning point in the profile at $x = 0.7440$. The change in shape of the velocity profile is characteristic for the separation of wall-bounded flows. Further, between positions $x = 0.7418$ and $x = 0.7430$, the first-order crosswise derivative at the wall approaches, but does not attain, the value zero signifying that flow separation is imminent. As the flow re-accelerates in the streamwise direction downstream of the wave trough (from $x = 0.7430$ to $x = 0.7456$) the second-order crosswise derivative of the velocity profile re-converges towards a negative value near the wall. Figure 7(*c*) shows the nucleus of the CSE forming at the wall slightly downstream of the point of minimal film thickness. Accordingly, the corresponding

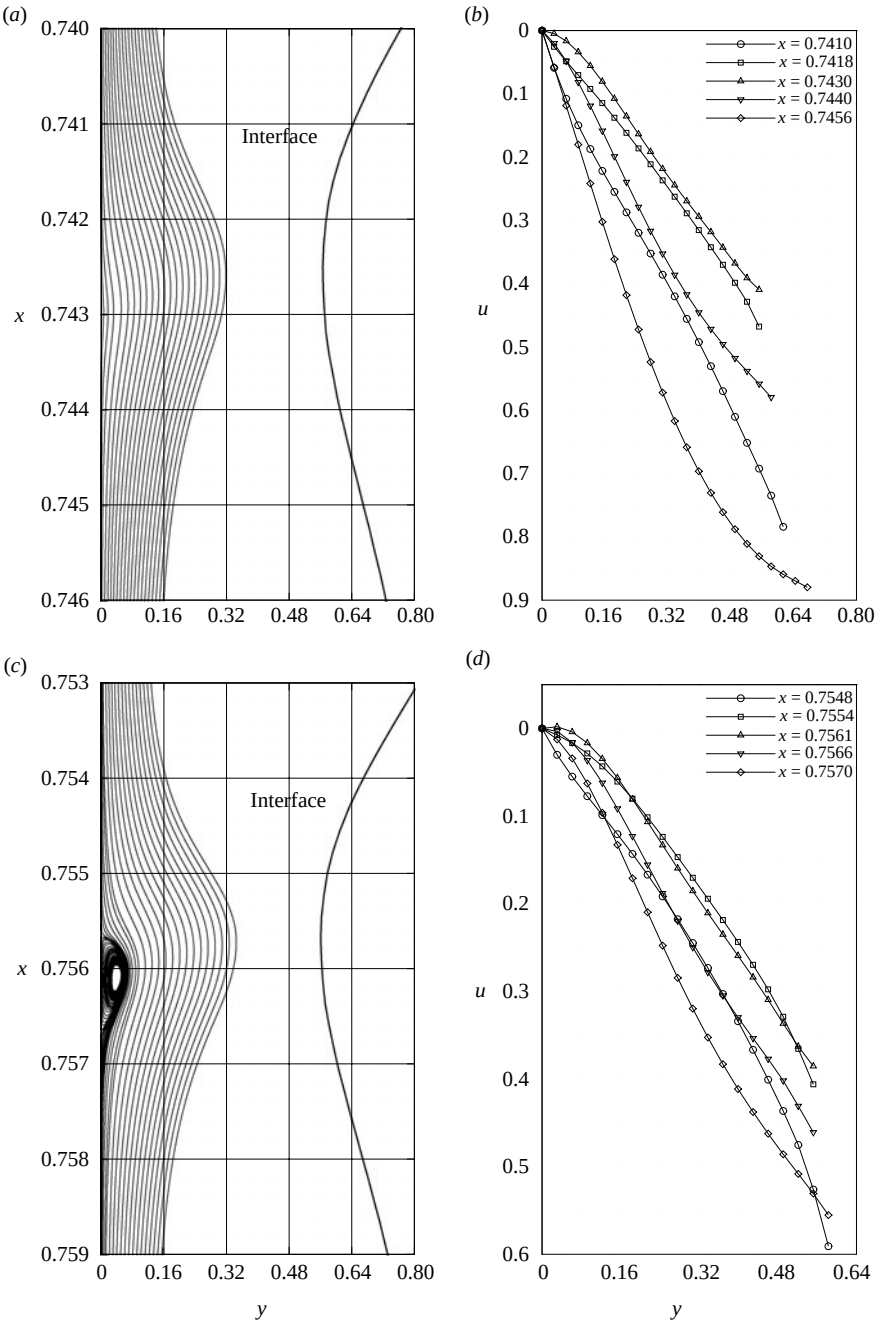

FIGURE 7. Near-wall streamlines and streamwise velocity profiles in the capillary-wave region. (*a*) Streamlines: $t = 0.741$; (*b*) velocity profiles: $t = 0.741$; (*c*) streamlines: $t = 0.747$; (*d*) velocity profiles: $t = 0.747$.

velocity profile at $x = 0.7561$ manifests a slightly negative value of the streamwise velocity component near the wall. The CSE subsequently grows attaining a crosswise size of about 50 % of the minimal film thickness (figure 8*a*). In particular, figure 8(*a*) shows that the flow is strongly influenced by the CSE at the crosswise position (i.e.

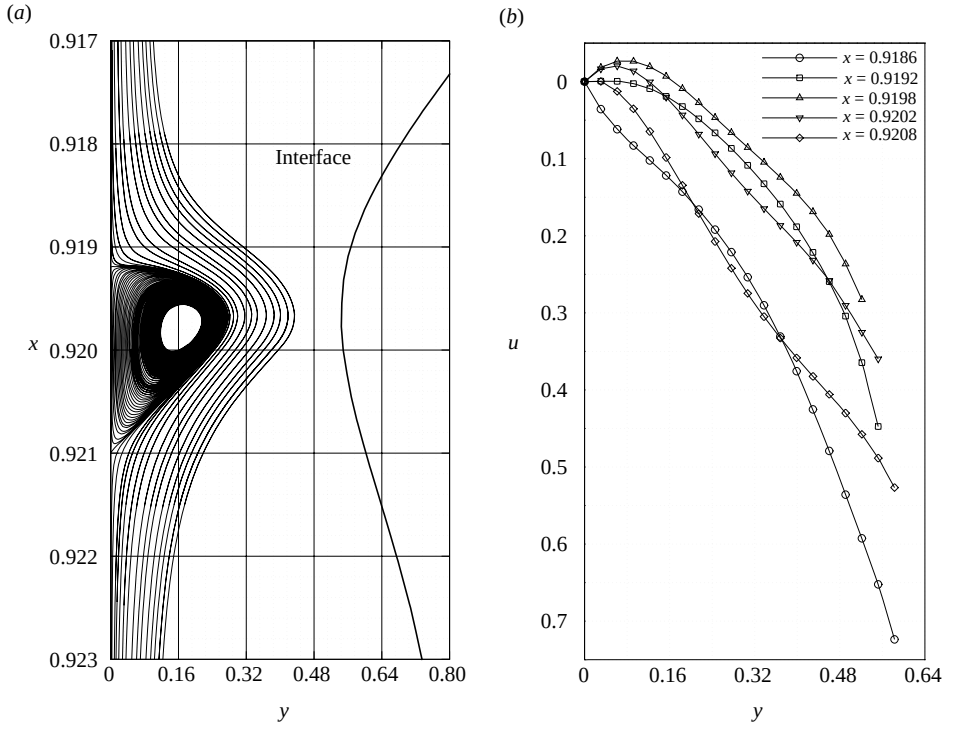

FIGURE 8. (*a*) Near-wall streamlines, $t = 0.819$, and (*b*) streamwise velocity profiles, $t = 0.819$, in the capillary-wave region.

$y = 0.309$) at which the velocity time traces were evaluated in figure 6(*a*). It therefore follows that the time trace of the streamwise velocity component depicted in figure 6(*a*) is associated with the existence of the CSE. Figure 8(*b*) shows the same qualitative behaviour of the near-wall velocity profile upstream of the CSE (between $x = 0.9186$ and $x = 0.9192$) as shown in figure 7(*b*). However, here the streamwise change in the shape of the near-wall profile is such that the threshhold of a vanishing first-order crosswise derivative at the wall is reached at $x = 0.9192$. At this position, the flow separation takes place. Downstream of the separation point between $x = 0.9198$ and $x = 0.9202$ the velocity profiles are characterized by a second root next to the one at the wall. Between the two roots, the streamwise velocity component is negative, confirming the flow reversal discernible in figure 8(*a*). Moving further downstream, the velocity profile re-approaches the pre-separation shape. Next to revealing regions of backflow, the profiles in figures 7(*b*) to 8(*b*) indicate the complexity of the velocity distribution in the capillary-wave region. Accurate models of wave dynamics based on long-wave theory have been published by Nguyen & Balakotaiah (2000), Ruyer-Quil & Manneville (2000), Mudunuri & Balakotaiah (2006) and Scheid *et al.* (2006). An essential assumption in their approach concerns the degree of freedom of polynomials representing the crosswise distribution of the streamwise velocity. The present results could serve as a physical justification of such modelling assumptions. To account for flow separation, polynomials representing the streamwise velocity component should obviously be at least of third order. This is not the case for lowest-order models which are based on a local approximation of the velocity profile with the solution for developed smooth film flow.

Case	Δ_x	Δ_y ($y < 1.855$)	Δ_y ($y > 1.855$)	Δt
1	4.545×10^{-4}	0.062	0.124	6.260×10^{-6}
2	2.273×10^{-4}	0.031	0.062	3.130×10^{-6}
3	1.136×10^{-4}	0.015	0.031	1.565×10^{-6}

TABLE 3. Dimensionless grid properties for investigated resolution variants.

Before proceeding with the analysis of the CSE, the adequacy of the spatial resolution of the numerical simulation is investigated. The agreement between numerical and experimental data presented in § 4.1 already serves toward the validation of the chosen discretization. However, such a comparison cannot be realized for all regions of the flow owing to the lack of experimental data in certain, less accessible regions. In particular, this applies to the region of the CSE. Consequently, the spatial and temporal discretization error in this region is investigated by way of a systematic variation of grid and time-step resolution. To reduce the computational burden, the employed computational domain is reduced in length to $L = 60\,\mathrm{mm}$ while the amplitude of the disturbance at the channel inlet is significantly increased. This forces the development of the CSE over a shorter distance. Table 3 displays the simulation properties for the investigated resolution variants. Figure 9(*a*) depicts the film thickness distribution in the capillary-wave region for the three resolution variants at the same point in time. It can be seen that the chosen spatial and temporal resolution (case 2) is of sufficient accuracy. Further, figures 9(*b*) to 9(*d*) depict corresponding streamline patterns along with the respective numerical grid. Results show that the size and position of the CSE does not change significantly for the two finest resolution variants, the finest grid revealing no new structures with respect to case 2. The coarsest resolution variant underpredicts the size of the CSE. In summary, the chosen spatial resolution for the numerical simulation (i.e. case 2) is adequate for the resolution of the CSE phenomenon.

From figures 7(*a*) to 8(*b*), it is clear that the phenomenon giving rise to the CSE is indeed that of near-wall flow separation (see e.g. Prandtl 1961; Sychev 1998). The occurrence of this phenomenon in falling liquid films, however, is at first unexpected and indeed the governing mechanism is different compared to classical boundary layer separation:

Concerning flow reversal in falling liquid films the first question coming to mind concerns the force causing such a behaviour. Arguably this governing force should act in the upstream direction. Considering that the wall parallel component of the gravitational force acts in the downstream direction and that viscosity forces are inner forces, only the pressure force can be retained as such. Thus, we can conclude that the CSE is induced by a positive pressure gradient in the capillary-wave region. This is in agreement with boundary-layer separation theory. However, in the latter case the pressure gradient is imposed on the boundary layer by the external flow. Bearing in mind that the falling liquid film considered here exists in a quiescent atmosphere, the positive pressure gradient causing the CSE must have a different origin. For falling liquid films, the positive pressure gradient in the liquid phase is imposed by surface tension forces which attain influence as a result of the distortion of the interface. This is shown in figures 10(*a*), 10(*c*) and 11(*a*) which depict the streamwise distribution of film thickness and static pressure difference $\Delta p = p - p_\mathrm{r}$ at the bounding wall. To understand these diagrams, the nature of the relation between film thickness

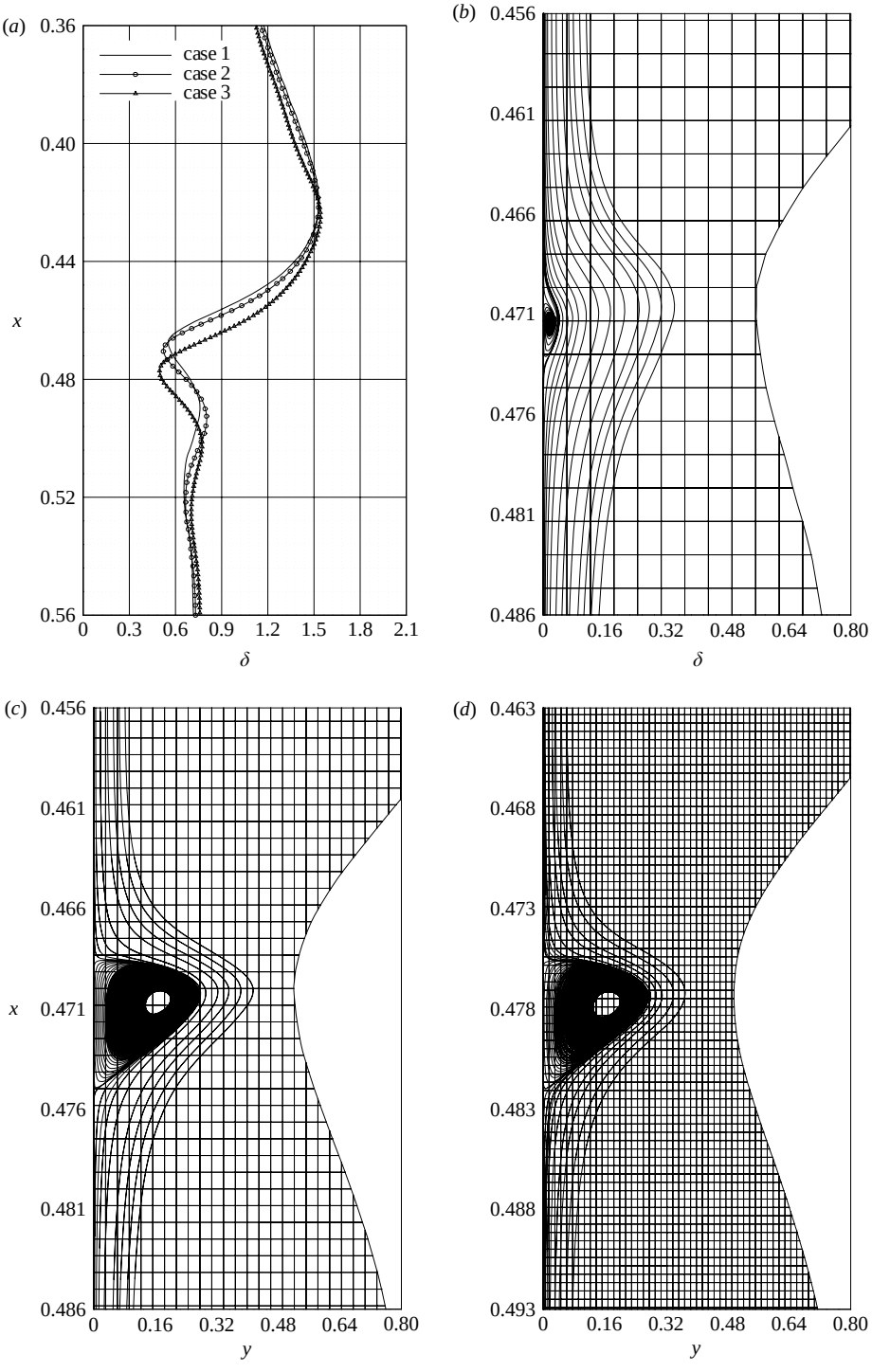

FIGURE 9. Comparison of numerical data for the resolution variants (cases 1 to 3) given in table 3. (*a*) Distributions of instantaneous film thickness over one wave. (*b*)–(*d*) Streamline patterns in the CSE region. (*b*) Case 1; (*c*) case 2; (*d*) case 3.

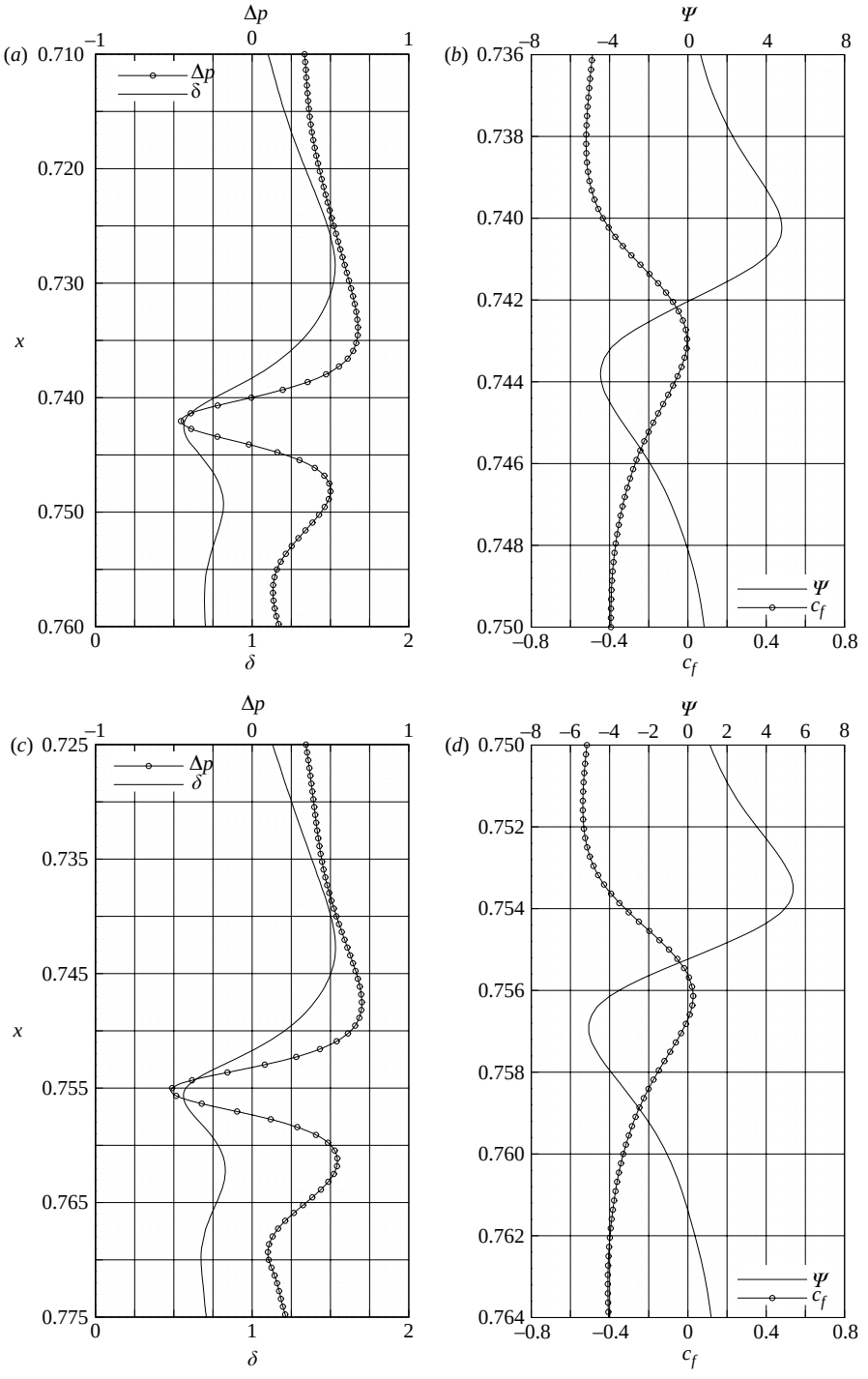

FIGURE 10. Numerical data corresponding to streamlines in figures 7(*a*) and 7(*c*). (*a*, *c*) Distribution of static wall pressure difference and film thickness for one wave. (*b*, *d*) Distribution of dimensionless wall shear stress and force ratio Ψ in the capillary-wave region (note change in ordinate scale). (*a*, *b*) $t = 0.741$; (*c*, *d*) $t = 0747$.

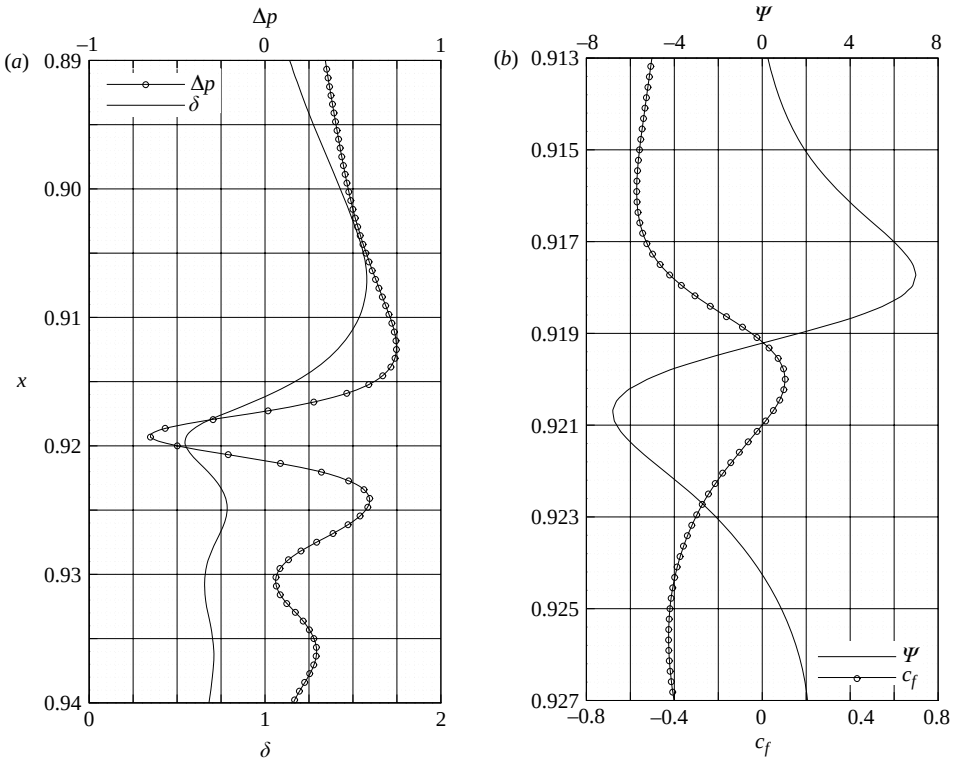

FIGURE 11. Numerical data corresponding to streamlines in figure 8(*a*). (*a*) Distribution of static wall pressure difference and film thickness for one wave. (*b*) Distribution of dimensionless wall shear stress and force ratio Ψ in the capillary-wave region (note change in ordinate scale). $t = 0.819$.

and pressure distribution in the liquid phase is recalled. Under the assumption of the dominance of pressure and surface tension forces and negligible gas pressure variation, the streamwise derivative of liquid pressure at the interface reduces to the following expression derived from the coupling condition in (3.4):

$$\frac{\partial p_l}{\partial x} = -\frac{\epsilon\, We}{3^{1/3}}\,\frac{\partial \kappa}{\partial x}, \quad \kappa = \frac{\epsilon\,(\partial^2\delta/\partial x^2)}{(1+\epsilon^2\,(\partial\delta/\partial x)^2)^{3/2}}, \tag{4.2}$$

where κ is introduced to designate the dimensionless interface curvature (subsequently referred to as interface curvature). For falling liquid films, owing to the small values of the crosswise velocity component, the dominant terms in the momentum equation in the crosswise direction are the pressure term and the gravitational term. Thus, for these flows, the pressure distribution on the wall is largely defined by the interface pressure distribution. It can thereby be concluded that the sign and absolute value of the streamwise pressure gradient at the wall are defined by the streamwise derivative of the interface curvature. It follows from the topological nature of surface waves that the pressure distribution in falling liquid films is always characterized by regions conducive to flow reversal. This corresponds to the conclusion that Kapitza & Kapitza (1965) come to, in a purely formal manner without considering the presence of capillary waves. Figures 10(*a*), 10(*c*) and 11(*a*) show that the conditions in the capillary-wave region are the most conducive to flow reversal. There, because of the small wavelength and large curvature of the capillary waves, large negative changes

in interface curvature (from positive to negative curvature) take place over a small distance. This leads to positive values of the streamwise pressure derivative at the wall which are significantly larger than in any other region of the flow. It is therefore understandable that the CSE develops in the capillary-wave region. The figures also show the temporal evolution of the pressure distribution at the wall as the capillary waves develop. An increase in the maximal positive value of the streamwise pressure gradient is discernible in figures 10(*a*), 10(*c*) and 11(*a*) as the capillary waves grow. This behaviour concurs with the episodes of flow deceleration, CSE nucleation and CSE growth (figures 7*a*, *c*, 8*a*). However, to assess the possibility of flow reversal it is not enough to investigate the pressure distribution along the wall. In fact, the resulting pressure force must be compared to the streamwise component of the gravitational force. Only if the former exceeds the latter, does the resulting streamwise external force act in the upstream direction, enabling flow reversal. In order to quantify this criterion, the ratio of the streamwise pressure force per unit volume to the streamwise gravitational force per unit volume Ψ (evaluated at the wall) as well as the dimensionless wall shear stress c_f:

$$\Psi = -\frac{\partial p}{\partial x} Fr^2 \epsilon, \quad c_f = -2\, Re\, \frac{\partial u}{\partial y}\bigg|_{y=0}, \tag{4.3}$$

are represented in figures 10(*b*), 10(*d*) and 11(*b*) for the points in time corresponding to figures 10(*a*), 10(*c*) and 11(*a*). The figures show that Ψ falls below the value -1 only in the capillary-wave region which thereby is the only one where flow reversal and thus the development of the CSE can take place. In figure 10(*b*), it is also discernible that flow reversal (indicated by a sign change in the dimensionless wall shear stress) does not take place as soon as Ψ falls below the value -1. However, after the CSE has attained a certain size the most upstream point of flow reversal coincides with the point at which Ψ attains the value -1 (figures 10*d*, 11*d*).

4.2.2. *Heat transfer enhancement due to the CSE*

Adomeit *et al.* (2000) and Kunugi & Kino (2005) show that the presence of the CSE significantly enhances heat transfer from the bounding wall to the liquid. The obvious explanation for this observation is the crosswise convective heat transfer induced by the CSE. Kunugi & Kino (2005) base this explanation on plots of the instantaneous velocity vector field showing the backflow in the capillary-wave region. This Eulerian approach could incorrectly suggest that the mixing length is of the order of the scale of the CSE. Because the wave velocity is considerably larger than the mean flow velocity in the residual layer, the conditions conducive to backflow are imposed for only a limited period by surface waves travelling over a given region of the film. Fluid elements are exposed only briefly to the annular streamlines of the CSE. To estimate the appropriate mixing length, a Lagrangian approach seems to be more suitable.

Figure 12(*a*) depicts path lines of fluid elements calculated from starting points equally distributed over the film thickness in the capillary-wave region. Path lines are calculated for a time interval ($t = 1.299$ to $t = 1.316$) corresponding to the transit of the capillary waves whereby the first and last point of each path line is associated with the corresponding bound of the time interval. Results show the fluid elements describing 'loop' or 'hook' shaped trajectories as the capillary waves pass over their position. Because of the decrease in flow velocity towards the wall, trajectories of fluid elements travelling near the wall are influenced at an earlier stage by the passing waves than those of fluid elements travelling further from the wall. Hence, the streamwise

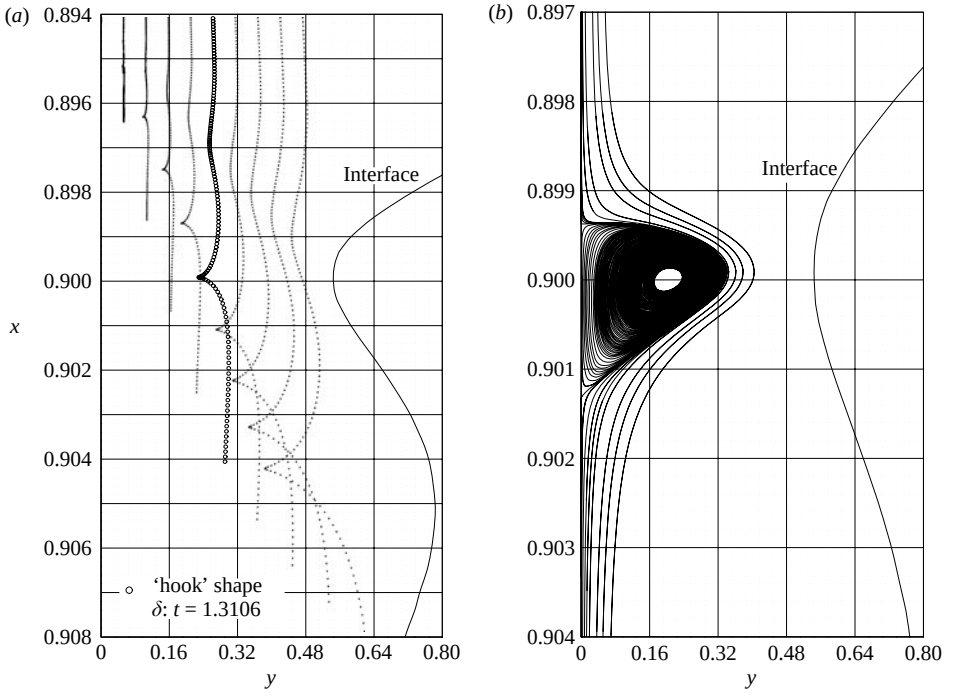

FIGURE 12. (*a*) Distribution of path lines computed for the transit of the CSE region ($t = 1.299$ to $t = 1.316$) and instantaneous film thickness for $t = 1.3106$. (*b*) Instantaneous streamline pattern in the CSE region for $t = 1.3106$ (note change in ordinate scale).

position of the characteristic 'loops' or 'hooks' moves downstream as the wall distance of the path line starting point increases. The film thickness distribution for the point in time ($t = 1.3106$) corresponding to the cusp in the highlighted 'hook' shaped path line is included in the graph. The associated streamline pattern is depicted in figure 12(*b*). Fluid elements travelling above the CSE centre follow 'hook' shaped path lines as they do not encounter flow reversal as opposed to near-wall elements which follow 'loop' shaped path lines. Figure 13(*a*) provides a close up view of 'loop' shaped path lines as these are not easily identifiable in figure 12(*a*). For this the near-wall region in figure 12(*a*) was magnified in the crosswise direction. Subsequently, path lines starting from points equally distributed over the magnified region were computed over the same time interval as for those depicted in figure 12(*a*). The streamwise extension of the region depicted in figure 13(*a*) is chosen such that all characteristic 'loops' are displayed. As near-wall fluid elements are reached by the travelling capillary waves at an early stage, this region is thus significantly shorter than in figure 12(*a*). Similar to figure 12(*a*), the characteristic 'loops' displayed in figure 13(*a*) shift in the streamwise direction with increasing wall distance.

The crosswise scale of the 'loops' or 'hooks' defines the local mixing length. This scale increases with the wall distance as the exposure time to the CSE conditions increases owing to the decreasing difference between wave velocity and flow velocity. Written in dimensionless form (using the appropriate scales defined in § 3.1) the effect on the mixing length l can be approximated as follows:

$$l = \tfrac{1}{2}\tilde{v}\Delta t \approx \tfrac{1}{2}\tilde{v}\frac{\Lambda}{(c_w - u)}, \tag{4.4}$$

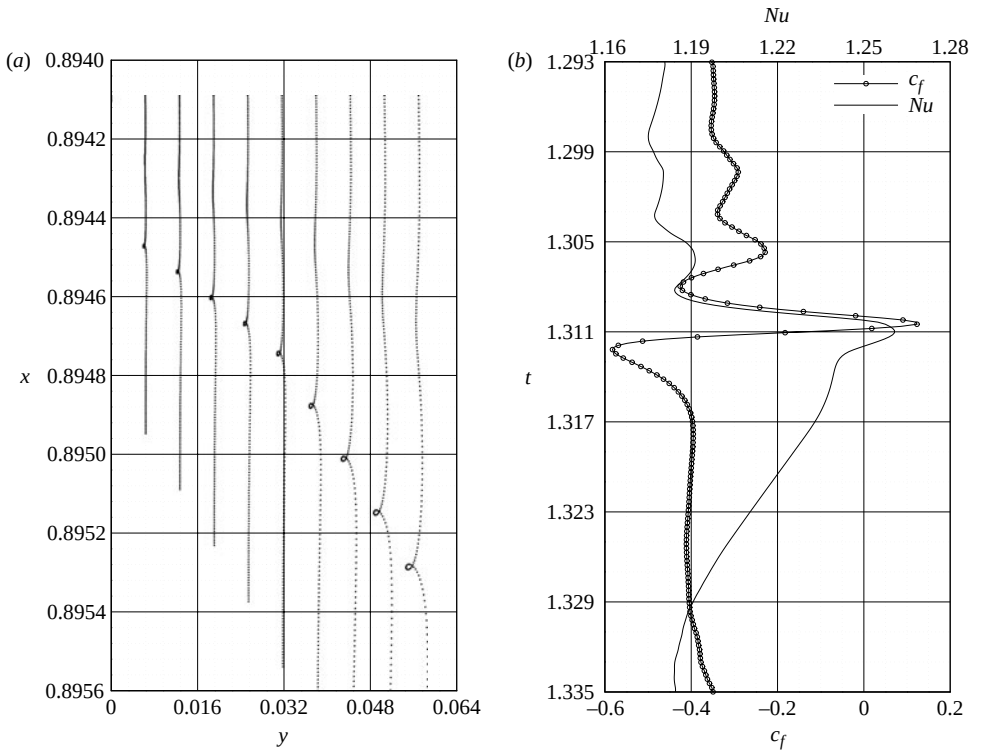

FIGURE 13. (*a*) Magnified view of the near-wall region in figure 12(*b*) showing loop-shaped path lines computed for the transit of the CSE region ($t = 1.299$ to $t = 1.316$). (*b*) Time traces of wall Nusselt number and dimensionless wall shear stress at $x = 0.9000$ in figure 12.

where $\tilde{v}$ designates the characteristic crosswise velocity induced by the CSE, c_w signifies the wave velocity, Λ the capillary wavelength and u the local streamwise velocity component prior to the wave transit which approximately satisfies a quadratic profile (see e.g. Alekseenko *et al.* 1994). Figure 13(*b*) depicts local time traces of the dimensionless wall shear stress c_f defined by (4.3) and the wall Nusselt number $Nu = -\partial\Theta/\partial y|_{y=0}$ evaluated at the streamwise position $x = 0.9000$. This position corresponds to that of the cusp in the highlighted 'hook' shaped path line in figure 12(*a*) so that the effect of the passing capillary wave on crosswise convective transport can be appreciated. Time traces were chosen over a spatial representation in order to isolate the effect of the CSE on heat transfer from effects due to the streamwise development of the temperature field. A change of sign in the dimensionless wall shear stress indicates the transit of the CSE region at the considered streamwise position. The figure shows that this coincides with a steep increase in the wall Nusselt number which attains its maximal value. After the transit of the CSE the Nusselt number remains high, decreasing to the value in the residual layer as the large wave moves by. For the regime investigated here, the CSE-induced increase of the Nusselt number is not as dramatic as reported by Kunugi & Kino (2005) and its influence on the temporally averaged Nusselt number is therefore not dominant. However, the onset of the heat transfer intensification is caused by the CSE. Further work is required to elucidate the contributions of the different mechanisms of heat transfer intensification in falling liquid films.

5. Conclusions

Spatially and temporally highly resolved numerical simulation of falling liquid film flow has been performed for a visco capillary regime. Attention has been directed to the elucidation of the backflow phenomenon arising in the region of capillary waves. Numerical results show that backflow develops as a result of flow separation at the wall in the residual layer of the film. The adverse pressure distribution inducing separation is imposed by the strong third-order deformation of the interface caused by capillary waves. Surface tension forces thereby act on the interface pressure jump as a result of the deformation. A necessary condition for separation is the compensation of the streamwise component of gravity by pressure forces. It has been shown that only in the region of capillary waves is the change in interface curvature of sufficient magnitude to cause the required adverse pressure distribution. Flow separation leads to a near-wall separation eddy varying in size as the capillary-wave profile develops. These results constitute the first mechanistic explanation of the backflow phenomenon to date. Numerical data were compared to experimental data to support the conclusions drawn. Comparison of numerical results with velocity time traces measured with laser-Doppler velocimetry yields good agreement. Characteristic features of time traces induced by the separation eddy are exhibited in both experimental and numerical data. Excellent agreement between experiment and simulation is obtained with respect to wave dynamics. The streamwise evolution of wave amplitude is predicted accurately by numerical simulation. Numerical and experimental time traces of film thickness in the developed region are also in agreement. Specifically the number, amplitude and period length of capillary waves is predicted accurately by the simulation. This serves as proof that the conditions conducive to flow separation are present in the case of falling liquid film flow. Further, the effect of the separation eddy on heat transfer from the wall to the liquid has been explained. Capillary waves travelling over the film substrate locally induce separation conditions for a time span depending on the difference between flow velocity and wave velocity. Therefore fluid elements are subjected to the annular streamlines in the separation eddy for only a limited time span. Resulting path lines are distorted in the crosswise direction owing to transiting capillary waves. The distortion is either 'loop' or 'hook' shaped depending on the wall distance of the considered fluid element. The resulting crosswise convective transport to and away from the wall is the cause of the well-documented increase of the heat transfer coefficient in the capillary-wave region. The scale of the path line distortion has been shown to be considerably smaller than the scale of the eddy and to increase with wall distance. Future investigations of the considered topic should concentrate on the derivation of a quantitative relation for the prediction of regimes characterized by backflow. Further a more detailed analysis of interaction between momentum and heat transfer in the region of backflow must be conducted with the goal of identifying regimes of optimal heat transfer. Further, the presented results seem to indicate that modelling approaches for heat transfer in the capillary-wave region on the basis of the mixing-length concept could prove successful. Finally, the investigation of capillary separation eddies in film flow with three-dimensional wave dynamics is desirable. There, both their effect on heat transfer and three-dimensional wave dynamics is of interest.

The authors would like to thank Professor Zeller and Professor Balakotaiah for helpful discussions and Mr Stratmann for his help with LDV experiments. The authors gratefully acknowledge the financial support of the Deutsche Forschungsgemeinschaft (DFG) within the Collaborative Research Center (SFB)

540 'Model-based Experimental Analysis of Kinetic Phenomena in Fluid Multi-phase Reactive Systems'.

REFERENCES

Adomeit, P., Leefken, A. & Renz, U. 2000 Experimental and numerical investigations on wavy films. In *3rd European Thermal Sciences Conf*., pp. 1003–1009. ETS, Heidelberg.

Albrecht, H. E., Borys, M., Damaschke, N. & Tropea, C. 2003 *Laser Doppler and Phase Doppler Measurement Techniques*. Springer.

Alekseenko, S. V., Nakoryakov, V. E. & Pokusaev, B. G. 1994 *Wave Flow of Liquid Films*. Begell House.

Benjamin, T. B. 1957 Wave formation in laminar flow down an inclined plane. *J. Fluid Mech.* **2**, 554–574.

Brackbill, J. U., Kothe, D. B. & Zemach, C. 1992 A continuum method for modelling surface tension. *J. Comput. Phys.* **100**, 335–354.

Brauer, H. 1956 Strömung und Wörmeübergang bei Rieselfilmen. *VDI Forschungsheft 457*, **22**.

Cohen-Sabban, J., Gaillard-Groleas, J. & Crepin, P.-J. 2001 Quasi-confocal extended field surface sensing. In *Proc. SPIE* (ed. A. Duparre & B. Singh), *Optical Metrology Roadmap for the Semiconductor, Optical, and Data Storage Industries II*, vol. 4449, pp. 178–183.

Davies, J. T. 1961 *Interfacial Phenomena*, pp. 267–268. Academic.

Elsäer, A. 1998 Kraftstoffaufbereitung in Verbrennungskraftmaschinen: Grundlagen der Strömung schubspannungsgetriebener Wandfilme. PhD thesis, Technische Universität Karlsruhe.

Friedman, S. J. & Miller, C. O. 1941 *Indust. Engng Chem. Fund.* **33**, 885.

Frisk, D. P. & Davis, E. J. 1972 The enhancement of heat transfer by waves in stratified gas–liquid flow. *Intl J. Heat Mass Transfer* **15**, 1537–1552.

Gao, D., Morley, N. B. & Dhir, V. 2003 Numerical simulation of wavy falling film flow using VOF method. *J. Comput. Phys.* **192**, 624–642.

Hirt, C. W. & Nichols, B. D. 1981 Volume of fluid (vof) method for the dynamics of free boundaries. *J. Comput. Phys.* **39**, 201–225.

Hjemfelt, A. T. & Mockros, L. F. 1966 Motion of discrete particles in a turbulent fluid. *Appl. Sci. Res.* **16**, 149.

Kapitza, P. L. 1948 Wave flow of thin layers of a viscous fluid (in russian). *Sov. Phys., J. Exp. Theor. Phys.* **3**, 3–28.

Kapitza, P. L. & Kapitza, S. P. 1965 Wave flow on thin layers of a viscous fluid: experimental study of undulatory flow conditions. In *Collected Papers of P. L. Kapitza* (ed. D. Ter Haar), vol. 2. Pergamon.

Kunugi, T. & Kino, C. 2005 DNS of falling film structure and heat transfer via mars method. *Comput. Struct.* **83**, 455–462.

Kunugi, T., Kino, C. & Serizawa, A. 2005 Surface wave structure and heat transfer of vertical liquid film flow with artificial oscillation. In *5th Intl Symp. Multiphase Flow, Heat Mass Ttransfer and Energy Conversion.*

Leefken, A. & Renz, U. 2001 Numerical analysis on hydrodynamics and heat transfer of laminar-wavy falling films. In *Proc. 1st Intl Berlin Workshop (IBW1) on Transport Phenomena with Moving Boundaries* (ed. F.-P. Schindler), vol. 738, pp. 134–143. VDI, Berlin.

Leefken, A., Al-Sibai, F. & Renz, U. 2004 LDV measurement of the velocity distribution in periodic waves of laminar falling films. In *Proc. 5th Intl Conf. on Multiphase Flow*.

Lel, V. V., Al-Sibai, F. & Leefken, A. 2005 Local thickness and wave velocity measurement of wavy films with a chromatic confocal imaging method and a fluorescence intensity technique. *Exps Fluids* **39**, 856–864.

Mudawar, I. & Houpt, R. A. 1993 Measurement of mass and momentum transport in wavy-laminar falling liquid films. *Intl J. Heat Mass Transfer* **36**, 4151–4162.

Mudunuri, R. R. & Balakotaiah, V. 2006 Solitary waves on thin falling films in the very low forcing frequency limit. *AIChE J.*

Nguyen, L. T. & Balakotaiah, V. 2000 Modeling and experimental studies of wave evolution on free falling viscous films. *Phys. Fluids* **12**, 2236–2256.

Nusselt, W. 1916 Der Wärmeaustausch am Berieselungskühler. *Zeitschrift des VDI* **67**, 206–210.

Portalski, S. 1964 Eddy formation in film flow down a vertical plate. *Indust. Engng Chem. Fund.* **3**, 49–53.

Prandtl, L. 1961 Über Flüssigkeitsbewegung bei sehr kleiner Reibung. In *Gesammelte Abhandlungen zur angewandten Mechanik, Hydro- und Aerodynamik* (ed. W. Tolmien, H. Schlichting & H. Görtler), vol. 2, chap. 4. Springer.

Ruyer-Quil, C. & Manneville, P. 2000 Improved modeling of flows down inclined planes. *Eur. Phys. J.* B **15**, 357–369.

Scheid, B., Ruyer-Quil, C. & Manneville, P. 2006 Wave patterns in film flows: modelling and three-dimensional waves. *J. Fluid Mech.* **562**, 183–222.

Sychev, V. V. 1998 *Asymptotic Theory of Separated Flows*. Cambridge University Press.

Takase, K., Yoshida, H., Ose, Y., Kano, T., Satake, S. & Kunugi, T. 2003 Large-scale numerical simulations of multiphase flow behavior in an advanced light-water reactor core. *Annu Rep. Earth Simulator Center.*

Whitham, G. B. 1974 *Linear and Nonlinear Waves.* John Wiley.

Wilke, W. 1962 Wärmeübergang an Rieselfilme. *VDI Fortschritte* **490**.

Youngs, D. L. 1982 *Numerical Methods in Fluid Dynamics*, pp. 273–285. Academic.